Excited State Band Mapping and Ultrafast Nonequilibrium Dynamics in Topological Dirac Semimetal 1T-ZrTe2

Sotirios Fragkos, Evgenia Symeonidou, Emile Lasserre, Baptiste Fabre, Dominique Descamps, Stéphane Petit, Polychronis Tsipas, Yann Mairesse, Athanasios Dimoulas, Samuel Beaulieu

NANO LETTERS

pubs.acs.org/NanoLett
Letter

Excited State Band Mapping and Ultrafast Nonequilibrium Dynamics in Topological Dirac Semimetal 1T-$ZrTe_2$

Sotirios Fragkos,* Evgenia Symeonidou, Emile Lasserre, Baptiste Fabre, Dominique Descamps, Stéphane Petit, Polychronis Tsipas, Yann Mairesse, Athanasios Dimoulas, and Samuel Beaulieu*

Cite This: *Nano Lett.* 2024, 24, 13397−13404

ABSTRACT: We performed time- and polarization-resolved extreme ultraviolet momentum microscopy on the topological Dirac semimetal candidate 1T-$ZrTe_2$. Excited state band mapping uncovers the previously inaccessible linear dispersion of the Dirac cone above the Fermi level. We study the orbital texture of bands using linear dichroism in photoelectron angular distributions. These observations provide hints about the topological character of 1T-$ZrTe_2$. Time-, energy-, and momentum-resolved nonequilibrium carrier dynamics reveal that intra- and interband scattering processes play a major role in the relaxation mechanism, leading to multivalley electron−hole accumulation near the Fermi level. We also show that electrons' inverse lifetime has a linear dependence as a function of their excess energy. Our time- and polarization-resolved XUV photoemission results shed light on the excited state electronic structure of 1T-$ZrTe_2$ and provide valuable insights into the relatively unexplored field of quantum-state-resolved ultrafast dynamics in 3D topological Dirac semimetals.

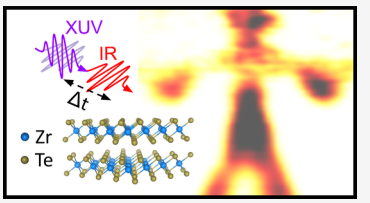

KEYWORDS: *Ultrafast Dynamics, Photoemission, Topological Materials, Dichroism, Electronic Structure, Molecular Beam Epitaxy*

Three-dimensional (3D) topological semimetals, including Dirac, Weyl, and nodal-line semimetals, have garnered significant interest, due to their unique electronic structures characterized by gapless topologically and symmetry-protected crossings between valence and conduction bands.[1,2] In Dirac semimetals, these crossings are protected by crystal rotational symmetry. They are formed through band inversion along the k_z direction of the three-dimensional Brillouin zone.[3]

Angle-resolved photoemission spectroscopy (ARPES) is widely considered the most advanced technique for examining the electronic structure of solids. As a result, ARPES has become a tool of choice for studying topological materials, which feature characteristic nontrivial bulk and surface states, e.g., topological surface states and Fermi arcs, which can be revealed using this technique.[4−9] The use of ultrafast laser pulses enables a new type of ARPES measurements (time-resolved ARPES, trARPES) that allows for the investigation of excited states and ultrafast dynamics in materials.[10] Although this technique has been extensively used on various topological materials, including Weyl semimetals,[11−14] topological insulators,[15−19] and graphene,[20−23] its application to 3D Dirac fermions has been limited.[24,25]

1T-$ZrTe_2$ was recently proposed to be a topological Dirac semimetal with a type-II crossing along the k_z direction.[26] Previous static ARPES studies had provided the first experimental evidence that few-layer 1T-$ZrTe_2$ epitaxially grown by molecular beam epitaxy (MBE) is a 3D topological Dirac semimetal.[27] More specifically, it was shown that linearly dispersing bands along the Γ−K and Γ−M directions cross near the Fermi level, indicating the existence of Dirac fermions, even down to the ultimate 2D limit of a single monolayer. In these measurements, the Dirac point was shown to be located at—or very close to—the Fermi level, which is notably different from the theoretical calculations that predict its location relatively far above it.[26−29] Despite these preliminary results on the electronic structure of 1T-$ZrTe_2$, its 3D topological Dirac semimetallic character has been a subject to debate. Indeed, synchrotron ARPES studies on single crystals of Cr-doped 1T-$ZrTe_2$[30] did not reveal clear Dirac-like features, unlike epitaxially grown thin films.[27] However, other studies combining synchrotron ARPES on 1T-$ZrTe_2$ single crystals with DFT calculations suggested that it is a Dirac semimetal,[28] but without direct observation of the Dirac crossing. Fermiology studies using de Haas−van Alphen oscillations have shown that 1T-$ZrTe_2$ exhibits no signature of nontrivial Berry phase.[29] This observation was attributed to the fact that the type-II Dirac cone could lie far above the Fermi level (∼500 meV).[29] On the other hand, recent magnetotransport measurements pointed toward the topological nature of 1T-$ZrTe_2$,[31−33] and a recent theoretical study using topological quantum chemistry predicted that 1T-$ZrTe_2$ is a topological Dirac semimetal.[34] However, since the Dirac crossing most probably lies above the Fermi level, accessing

Received: August 19, 2024
Revised: October 4, 2024
Accepted: October 4, 2024
Published: October 9, 2024

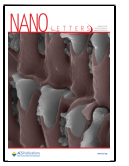

https://doi.org/10.1021/acs.nanolett.4c04019
Nano Lett. 2024, 24, 13397−13404

these subtle features with static ARPES poses significant challenges. Excited state band mapping using trARPES represents a potential solution to this issue.

In this study, we perform time- and polarization-resolved extreme ultraviolet (XUV) momentum microscopy on the 1T-$ZrTe_2$ topological Dirac semimetal candidate. By photoexciting electrons into high-lying conduction bands using infrared pump pulses (1030 nm, 1.2 eV), we uncover the energy-momentum dispersion of the electronic band structure above the Fermi level. Furthermore, the linear dichroism in photoelectron angular distributions (LDAD) obtained from polarization-resolved measurements on the photoexcited 1T-$ZrTe_2$ allows us to reveal different orbital textures of bands in an extended energy-momentum range, typically inaccessible using conventional dichroic ARPES measurements. Second-derivative analysis of the photoemission intensity shows that the Dirac cone crosses the conduction band ∼250 meV above the Fermi level. Moreover, energy- and momentum-resolved ultrafast carrier dynamics reveal that photoexcited electrons' inverse lifetime has a linear dependence on the excess energy. Our time- and quantum-state-resolved ultrafast electron and hole dynamic measurements allow us to unveil microscopic processes, including intra- and intervalley scattering, governing the nonequilibrium dynamics in photoexcited 3D topological Dirac semimetals.

Figure 1(a) shows a schematic of the experimental geometry. An s-polarized infrared (IR, 1.2 eV, 135 fs, 2.95 mJ/cm^2) pump and polarization-tunable (s- or p-polarized) XUV (21.6 eV) probe pulses are superimposed onto the 1T-$ZrTe_2$ sample at room temperature in the interaction chamber of the time-of-flight momentum microscope. The 1T-$ZrTe_2$

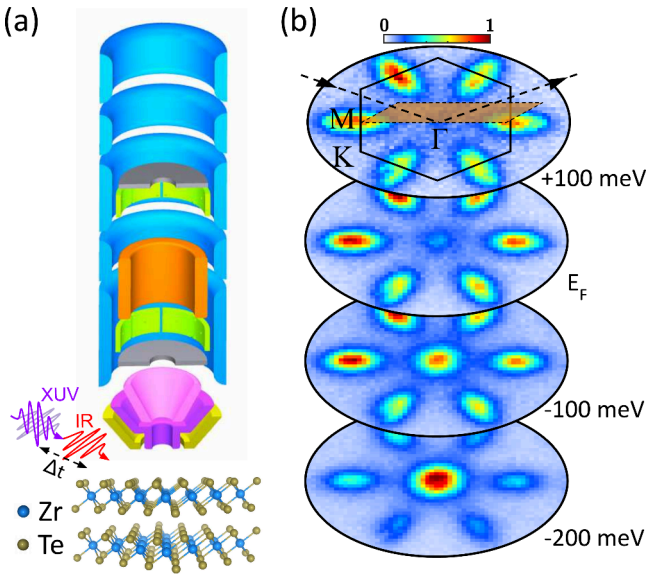

Figure 1. Schematic of the experiment. (a) An infrared pump and a polarization-tunable (s- or p-polarized) XUV (21.6 eV) probe pulses are focused onto an MBE-grown 1T-$ZrTe_2$ sample, in the interaction chamber of a time-of-flight momentum microscope, at an incidence angle of 65°. (b) Constant energy contours for different binding energies, obtained by summing photoemission intensities measured with s- and p-polarized XUV. These measurements were taken at the pump−probe temporal overlap, with an s-polarized IR pump pulse (1.2 eV, 135 fs, 2.95 mJ/cm^2). The light scattering plane (orange tilted rectangle overlaid with CEC in (b)) is aligned with the crystal mirror plane $\mathcal{M}$, i.e., is along the Γ−M direction.

samples were grown by MBE on the Si(111)/InAs(111) substrates. More information about the experimental setup and sample preparation can be found in the Supporting Information and elsewhere.[27,35,36]

$ZrTe_2$ belongs to the 1T transition metal dichalcogenide layered octahedral family with space group $P\bar{3}m1$ (No. 164). It is anticipated that the 3D gapless Dirac crossing originates from two bands associated with different irreducible representations, which prohibit gap opening due to hybridization. Theoretical calculations have predicted a pair of 4-fold degenerate Dirac nodes ∼500 meV above the Fermi level, at (k_x = 0, k_y = 0, k_z = ±0.228c*) momenta,[26] where c* is the inverse out-of-plane lattice constant. These Dirac nodes are protected by the C_3 rotational symmetry along the c axis. Figure 1(b) also shows constant energy contours for different binding energies, obtained by summing photoemission intensities obtained with s- and p-polarized XUV, at pump−probe overlap with the s-polarized pump pulse.

The energy- and momentum-dependence of the photoemission transition dipole matrix element holds valuable information about wave functions underlying the electronic band structure. Notable examples include the orbital character of the electronic band structure[16,37−40] as well as Berry curvature,[41−44] which are probed by the modification of photoemission intensities upon the modulation of the polarization state of the ionizing radiation, in a scheme referred to as dichoic ARPES. In that spirit, we performed polarization-resolved measurements at pump−probe overlap (Δt = 0 fs), by measuring the energy- and momentum-resolved photoemission intensity while continuously rotating the XUV linear polarization axis angle. A cut of the photoemission intensity along M−Γ−M, integrated over all XUV polarization states, is shown in Figure 2(a). Figures 2(c),(d) show the normalized (for each energy) photoemission intensities along the same high-symmetry cut for s- and p-polarized XUV pulses. One can notice striking differences between these two configurations. Indeed, with s-polarized XUV, a linear Dirac band extending a few 100 meV above the Fermi level is probed around Γ, while with p-polarized XUV, the Dirac band is absent and a parabolic hole-like band appears. Additionally, the contribution of the electron-like pockets at M points is strongly enhanced with p-polarized XUV. A previous polarization-dependent synchrotron-ARPES study on 1T-$ZrTe_2$ has shown similar photoemission intensity modulation upon changing polarization and attributed this behavior to the different orbital character of the bands below the Fermi level.[28] Additionally, the orbital-resolved band structure calculations reported in this study predicted that the parabolic band at Γ and electron-like M pockets are mostly composed of orbitals with out-of-plane characters (Te p_z and Zr d_{z^2}, respectively), while the tip of the Dirac cone is composed of Zr d_{xz} and d_{yz} orbitals. The XUV LDAD presented in Figure 2(b) is in good agreement with the above-mentioned predictions. Indeed, at strong off-normal geometry (angle of incidence of 65°), p-polarized light is expected to favor photoemission from out-of-plane orbitals. In addition, our pump−probe scheme also allows accessing LDAD of states above the Fermi level, which is not possible using static polarization-resolved ARPES. This enables us to extract simultaneously the LDAD from the M pockets, the parabolic band at Γ (red color), and the tip of the linear Dirac cone dispersing above the Fermi level around the Γ point (blue color). It is thus evident that the photoemission transition dipole matrix elements significantly influence the ARPES

https://doi.org/10.1021/acs.nanolett.4c04019
Nano Lett. 2024, 24, 13397−13404

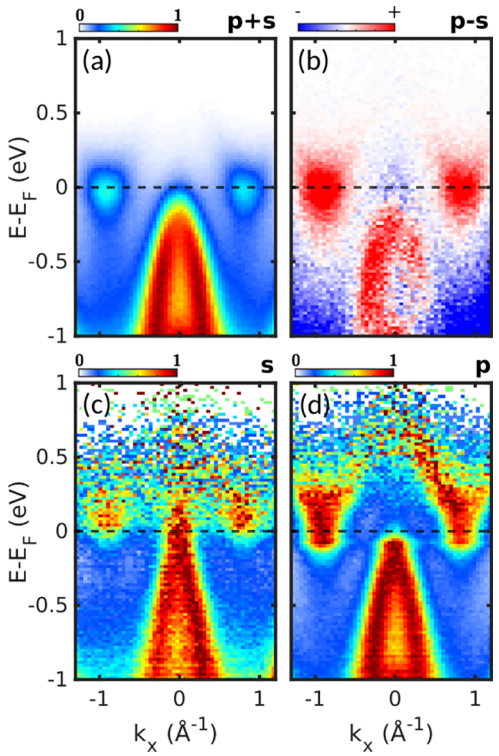

Figure 2. Linear dichroism in photoexcited 1T-$ZrTe_2$. Band structure mapping of 1T-$ZrTe_2$ along the M−Γ−M direction, at pump−probe overlap (Δt = 0 ps), using an s-polarized pump pulse to avoid the spurious effect of laser-assisted photoemission. (a) Raw signal (unnormalized) obtained by summing photoemission intensities measured using an s- and p-polarized XUV probe pulse. (b) XUV LDAD extracted by subtracting the photoemission intensities measured using p- and s-polarized XUV probe pulses. (c) Normalized photoemission intensity measured using s-polarized XUV probe pulses. (d) Normalized photoemission intensity measured using p-polarized XUV probe pulses. In (c) and (d), each momentum-resolved energy slice of the photoemission intensity is normalized by its maximum value.

spectra of 1T-$ZrTe_2$ and that s-polarized XUV substantially enhances the photoemission intensity from the Dirac cone.

To gain a deeper insight into the dispersion of the Dirac cone, high-statistic measurement was conducted at pump−probe overlap (Δt = 0 fs) with s-polarized XUV (Figure 3(a)). The associated photoemission intensity along the M−Γ−M direction shows a clear Dirac-like cone extending far above the Fermi level. Second derivative analysis of this signal (Figure 3(b)) (more details about the second derivative analysis procedure are given in the Supporting Information, Figure S2) indicates that the electron-like conduction bands with minima at M points disperse upward toward the Γ point, merging with the tip of the Dirac cone at ∼250 meV above the Fermi level. An electron-like band at Γ can also be seen above this crossing (around 0.6 eV < $E - E_F$ < 1 eV). These observations are in good agreement with previously reported calculations, which predict that 1T-$ZrTe_2$ is a 3D topological Dirac semimetal.[26−29] It is important to note that the Dirac bands also exhibit dispersion along the k_z axis, and accurate determination of the position of the Dirac point in the 3D Brillouin zone would require photon-energy-dependent[5,6,45] trARPES measurements. While this is currently not possible with our setup, time-resolved ARPES with XUV photon-energy tunability are now emerging[46−51] and could be very useful to probe the 3D dispersion of electronic states above the Fermi level. However, this type of experiment represents a major challenge.

After meticulously analyzing the excited state dispersion and orbital characters, we now focus on the ultrafast nonequilibrium carrier dynamics in photoexcited 1T-$ZrTe_2$. We performed pump−probe measurements with an s-polarized IR pump, to avoid spurious effects of laser-assisted photoemission during the optical cross-correlation, and s-polarized XUV pulses to efficiently access the ultrafast dynamics of carriers within the Dirac cone. Figure 4(a) shows the energy- and

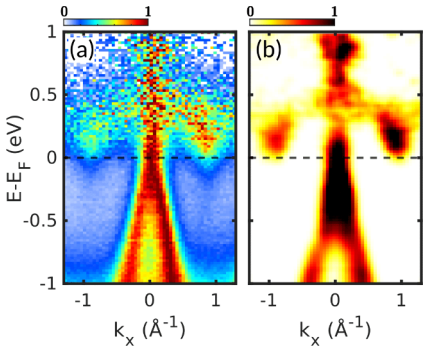

Figure 3. Excited state band mapping. (a) Normalized energy-momentum cut along the M−Γ−M direction at pump−probe overlap (Δt = 0 ps). The IR pump and the XUV probe are s-polarized. (b) Second derivative analysis of the energy-momentum cut along the M−Γ−M direction shown in (a). The second derivative presented in (b) is calculated by summing the second derivatives along the momentum and energy axes. More details about the second derivative procedure can be found in the Supporting Information.

momentum-resolved differential map along M−Γ−M high-symmetry directions, generated by subtracting the photoemission intensity obtained before (integration between −1.25 and −0.95 ps) and during/after (integration between 0 and +0.3 ps) optical photoexcitation. Negative differential photoemission intensity (blue color) mainly results from the hole creation upon optical photoexcitation and subsequent intra- and interband scattering processes. Conversely, positive differential photoemission intensity (red color) mainly originates from electron creation upon optical photoexcitation and subsequent scattering processes. Excitation-induced band renormalizations can also leave their imprint onto these differential maps.[12−14] However, under these experimental conditions, we did not observe any significant band renormalization between the equilibrium and the photoexcited states of the sample.

In the differential map (Figure 4(a)), we observe a very faint positive signal centered around Γ and extending up to ∼1 eV above the Fermi level. This indicates that vertical optical transitions induced by the IR pump occur between the Dirac cone and the high-lying excited states around Γ. These hot electrons can subsequently relax through intra- and interband scattering and accumulate near the Fermi level within the tip of the Dirac cone at Γ and within M pockets, leading to a strong positive (red) signal. In addition, we observe significant hole accumulation just below the Fermi level, both within the Dirac cone at Γ and within M pockets. The creation of holes at M pockets most likely arises from phonon-assisted M−Γ intervalley scattering since there is no pair of bands allowing direct optical transition with a 1.2 eV photon near M points.

https://doi.org/10.1021/acs.nanolett.4c04019
Nano Lett. 2024, 24, 13397−13404

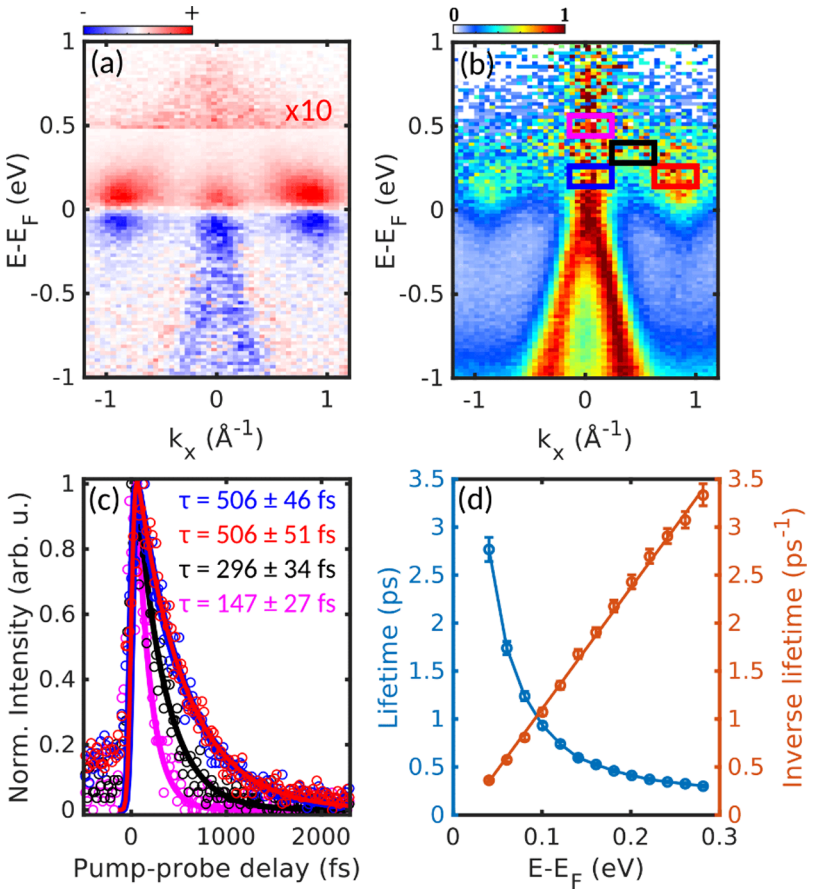

Figure 4. Energy- and momentum-resolved ultrafast nonequilibrium dynamics. (a) Energy- and momentum-resolved differential map, generated by subtracting the photoemission intensity obtained before (integration between −1.25 ps and −0.95 ps) and during/after (integration between 0 ps and +0.3 ps) optical photoexcitation. This differential map was obtained by summing photoemission intensities for all three M−Γ−M directions of the Brillouin zone to enhance statistics. (b) Energy-momentum cut along the M−Γ−M direction with integration boxes used in (c), where energy- and band-resolved temporal evolution of the photoexcited electrons within these regions of interest are shown. (d) Momentum-integrated electron population lifetimes and associated inverse lifetimes as a function of excess energy.

The temporal evolution of photoexcited electrons within various energy-momentum regions of interest (ROI, squares in Figure 4(b)) is depicted in Figure 4(c), revealing the energy- and band-resolved ultrafast electron dynamics. Surprisingly, the extracted lifetime (∼500 fs) at the tip of the Dirac cone above the Fermi level at Γ (blue ROI box) is the same as the one extracted at the M pocket (red ROI box), at the same energy (between 0.14 and 0.26 eV), which implies that the carrier lifetime seems to be momentum-independent. This suggests that interband scattering processes that are faster than our temporal resolution (∼140 fs) are at play, leading to an apparent momentum-independent carrier lifetime. For higher energy electrons (between 0.44 and 0.56 eV, pink ROI box), the extracted lifetime decreases to ∼150 fs. In addition, looking at time-resolved photoemission intensity in regions of interest symmetric in energy with respect to the Fermi level (below and above) reveals remarkably similar decay dynamics for electrons and holes (Figure S3). This charge compensation between electron and hole pockets, even in nonequilibrium settings, was also observed in type-II Weyl semimetallic WTe_2 and was argued to be a key effect in explaining the nonsaturating magnetoresistance of this type of material.[52]

Having established the momentum-independent behavior of the ultrafast carrier lifetime, we can now extract the momentum-integrated (integrated for all momenta), energy-resolved lifetime of photoexcited electrons (Figure 4(d)). For electrons near the Fermi level ($E - E_F$ = 40 meV), the population lifetime is relatively long, i.e., ∼3 ps, while for high-energy electrons ($E - E_F$ = 280 meV), the lifetime is as small as ∼300 fs. Indeed, the inverse lifetime increases linearly as a function of excess energy, with a slope of 12.6 ± 0.4 ps^{-1} eV^{-1}, as one can see in Figure 4(d). This linear dependence of the inverse lifetime as a function of excess energy was already observed in other semimetals,[24,25] where the electron−phonon coupling strength g was derived from this slope (S), using the equation $S = g(T_e - T_L)/(2C_e k_B T_e)$, where C_e is the electron heat capacity, T_e is the transient electronic temperature, and T_L is the lattice temperature. Determining electron−phonon coupling strength g using energy-resolved lifetime measurements thus requires knowledge about the electron heat capacity C_e, which, to the best of our knowledge, has not yet been reported for 1T-$ZrTe_2$. Moreover, this unconventional non-Fermi-liquid behavior of the electron inverse lifetime as a function of excess energy has been predicted in layered materials, such as graphite.[53] This phenomenon arises from the combined effects of linearly dispersing bands near the Fermi level and reduced Coulomb screening. A similar behavior has also been observed in the excitonic insulator candidate Ta_2NiSe_5, which features a quasi-linearly dispersing conduction band.[54] In this material, the non-Fermi-liquid electron inverse

https://doi.org/10.1021/acs.nanolett.4c04019
Nano Lett. 2024, 24, 13397−13404

lifetime as a function of excess energy was also shown to increase with excitation density due to transient screening.[54] In the case of 1T-$ZrTe_2$, low dimensionality and reduced screening likely play significant roles in determining the photoexcited electron lifetime.

Even though we cannot extract the electron−phonon coupling strength from our energy-resolved lifetime measurements, we can compare the ultrafast carrier dynamics in 1T-$ZrTe_2$ with similar measurements performed on other topological semimetals. In the Dirac nodal line semimetal $PtSn_4$, an ultrafast population lifetime as short as 400 fs was observed for electrons 100 meV above the Fermi level. This short population lifetime results from multichannel electron−phonon scattering among its complex metallic bands.[25] In $PtSn_4$, the slope extracted from the inverse lifetime as a function of excess energy is around ∼14 ps^{-1} eV^{-1},[25] a value similar to the one we obtained for 1T-$ZrTe_2$. Conversely, in 3D type-I Dirac semimetal Cd_3As_2, a significantly longer carrier lifetime of ∼3 ps for electrons 100 meV above the Fermi level and a slope of ∼2 ps^{-1} eV^{-1} (inverse lifetime as a function of excess energy) were measured.[24] It was argued that carrier lifetime in Cd_3As_2 is significantly longer than in, for example, 2D Dirac fermions in graphene because of lower optical phonon energy. In 1T-$ZrTe_2$, at the same energy (100 meV above Fermi level), the electron lifetime is ∼1 ps, i.e., in between lifetimes measured for $PtSn_4$ and Cd_3As_2. To explain this behavior, scattering phase space arguments can be used. Indeed, type-I Dirac semimetals have nearly zero density of states (DOS) at the Dirac point, which strongly restricts the scattering phase space for electron−hole recombination. This can explain the long lifetime observed in Cd_3As_2 and is also at the origin of population inversion in this material, i.e., the Dirac point acting as a bottleneck for the ultrafast carrier relaxation.[24] In 1T-$ZrTe_2$, the ultrafast decay mechanism is more complex, since neighboring (non-Dirac) bands also allow for interband scattering processes, similar to the case of $PtSn_4$. Moreover, a trARPES study on $MoTe_2$ and WTe_2 type-II Weyl semimetals reported an ultrafast population lifetime of ∼465 fs and ∼1180 fs, respectively, for electrons slightly above the Fermi level.[12] These fast population lifetimes, on the same order of magnitude as the ones obtained for $PtSn_4$ and 1T-$ZrTe_2$, likely originate from the relatively large electron and hole DOS near the Fermi level. Therefore, the shorter lifetime and the absence of population inversion can be associated with larger phase space available for electron−hole scattering and recombination. In addition, these observations could also be linked to the nature of the topological crossing in 1T-$ZrTe_2$. As mentioned above, 1T-$ZrTe_2$ is predicted to be a type-II Dirac semimetal.[26,28,29] In contrast to type-I, type-II Dirac and Weyl semimetals have a nonzero DOS at the Dirac/Weyl points, since they appear as the touching point between strongly tilted electron and hole pockets. Therefore, a type-II Dirac crossing could not act as a bottleneck for the relaxation of photoexcited electrons.

In Figure 5, we summarize the main steps underlying the ultrafast carrier dynamics in 1T-$ZrTe_2$, which were revealed by using our time- and polarization-resolved momentum microscopy measurements. The IR pump pulse induces vertical interband transitions (vertical dashed gray arrows), creating photoholes (small blue circles) in the band manifold near Γ below the Fermi level, and excited electrons (small red circles) in high-lying bands at associated momentum. This photoexcitation triggers a cascade of intra- and interband scattering

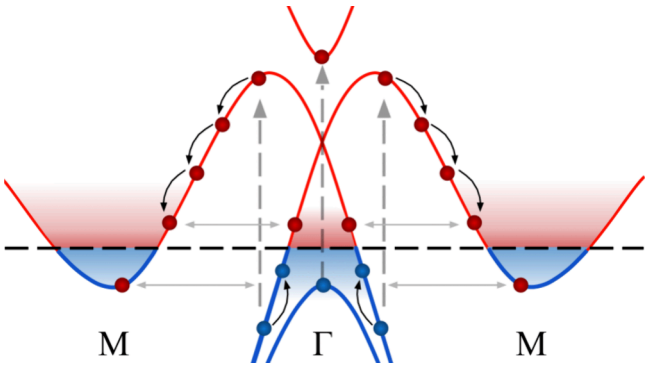

Figure 5. Schematic of ultrafast nonequilibrium carrier dynamics in 1T-$ZrTe_2$. The vertical dashed gray lines represent optical transitions leading to initial electron and hole creation. The horizontal light gray arrow represents interband transitions, while the curved black arrows represent intravalley scattering. Shaded red and blue areas represent the accumulation of electrons and holes, above and below the Fermi level.

events that bring the system back toward equilibrium. Indeed, hot electrons can scatter to lower energies, filling the tip of the Dirac cone at Γ and M pockets near the Fermi level. Concomitantly, intervalley scattering between Γ and M bands allows reshuffling the hole population below the Fermi level. Multivalley electron−hole recombination can thus bring back the electronic system to equilibrium, on a few picosecond time scale.

In conclusion, our time- and polarization-resolved XUV momentum microscopy of 1T-$ZrTe_2$ allowed us to reveal the previously inaccessible linear dispersions of the bulk Dirac cone above the Fermi level. The linear dichroism in photoelectron angular distributions from photoexcited 1T-$ZrTe_2$ enabled us to unveil different orbital textures of bands below and above the Fermi level, which is beyond the reach of conventional dichroic ARPES measurements. Excited state band mapping combined with linear dichroism hints at the topological character of the electronic states of this material. We determined the position of the Dirac point, which is located ∼250 meV above the Fermi level. Ultrafast time-, energy-, and momentum-resolved photoemission measurements using well-chosen IR pump and XUV probe polarization states allowed us to provide a quantum-state-resolved picture of scattering processes governing the out-of-equilibrium behavior of this topological Dirac semimetal. We showed that both intra- and interband scattering processes play a major role in ultrafast carrier relaxations, leading to multivalley electron−hole accumulation near the Fermi level. In addition, the momentum-integrated inverse lifetime shows a linear dependence, as in other Dirac and nodal-line semimetals. Our work sheds light on the previously experimentally unmapped excited states of 1T-$ZrTe_2$ and provides insights into the relatively unexplored field of ultrafast dynamics in 3D topological Dirac semimetals.

■ ASSOCIATED CONTENT

Supporting Information

The Supporting Information is available free of charge at https://pubs.acs.org/doi/10.1021/acs.nanolett.4c04019.

Additional discussions and/or figures about the experimental setup, growth methodology, decapping process, band structure mapping, and second derivative

https://doi.org/10.1021/acs.nanolett.4c04019
Nano Lett. 2024, 24, 13397−13404

analysis, balanced ultrafast electron and hole dynamics, as well as momentum-independent carrier lifetime analysis (PDF)

AUTHOR INFORMATION

Corresponding Authors

Sotirios Fragkos − *Université de Bordeaux - CNRS - CEA, CELIA, UMR5107, F33405 Talence, France*; Email: sotirios.fragkos@u-bordeaux.fr

Samuel Beaulieu − *Université de Bordeaux - CNRS - CEA, CELIA, UMR5107, F33405 Talence, France*; orcid.org/0000-0003-2316-2224; Email: samuel.beaulieu@u-bordeaux.fr

Authors

Evgenia Symeonidou − *Institute of Nanoscience and Nanotechnology, National Center for Scientific Research "Demokritos", 15310 Athens, Greece; School of Chemistry, Aristotle University of Thessaloniki, 54124 Thessaloniki, Greece*

Emile Lasserre − *Université de Bordeaux - CNRS - CEA, CELIA, UMR5107, F33405 Talence, France*

Baptiste Fabre − *Université de Bordeaux - CNRS - CEA, CELIA, UMR5107, F33405 Talence, France*; orcid.org/0000-0001-9843-8139

Dominique Descamps − *Université de Bordeaux - CNRS - CEA, CELIA, UMR5107, F33405 Talence, France*

Stéphane Petit − *Université de Bordeaux - CNRS - CEA, CELIA, UMR5107, F33405 Talence, France*

Polychronis Tsipas − *Institute of Nanoscience and Nanotechnology, National Center for Scientific Research "Demokritos", 15310 Athens, Greece*; orcid.org/0000-0001-9064-9601

Yann Mairesse − *Université de Bordeaux - CNRS - CEA, CELIA, UMR5107, F33405 Talence, France*; orcid.org/0000-0002-9098-7421

Athanasios Dimoulas − *Institute of Nanoscience and Nanotechnology, National Center for Scientific Research "Demokritos", 15310 Athens, Greece*; orcid.org/0000-0003-3199-1356

Complete contact information is available at: https://pubs.acs.org/10.1021/acs.nanolett.4c04019

Notes

The authors declare no competing financial interest.

ACKNOWLEDGMENTS

We thank Nikita Fedorov, Romain Delos, Pierre Hericourt, Rodrigue Bouillaud, Laurent Merzeau, and Frank Blais for technical assistance. We thank Gerd Schönhense, Olena Tkach, and Sergey Babenkov for stimulating discussions regarding momentum microscopy. This study received financial support from the French government in the framework of the University of Bordeaux's France 2030 program/GPR LIGHT. We acknowledge the funding from MSCA-ITN project SMART-X-860553. We acknowledge support from ERC Starting Grant ERC-2022-STG No.101076639, Quantum Matter Bordeaux, AAP CNRS Tremplin and AAP SMR from Université de Bordeaux. The research leading to these results has received funding from LASERLAB-EUROPE (grant agreement no. 871124, European Union's Horizon 2020 research and innovation programme). This work was funded by the European Union. Views and opinions expressed are however those of the author(s) only and do not necessarily reflect those of the European Union. Neither the European Union nor the granting authority can be held responsible for them.

REFERENCES

(1) Armitage, N. P.; Mele, E. J.; Vishwanath, A. Weyl and Dirac semimetals in three-dimensional solids. *Rev. Mod. Phys.* **2018**, *90*, 015001.

(2) Lv, B. Q.; Qian, T.; Ding, H. Experimental perspective on three-dimensional topological semimetals. *Rev. Mod. Phys.* **2021**, *93*, 025002.

(3) Yang, B.-J.; Nagaosa, N. Classification of stable three-dimensional Dirac semimetals with nontrivial topology. *Nat. Commun.* **2014**, *5*, 4898.

(4) Xia, Y.; Qian, D.; Hsieh, D.; Wray, L.; Pal, A.; Lin, H.; Bansil, A.; Grauer, D.; Hor, Y. S.; Cava, R. J.; Hasan, M. Z. Observation of a large-gap topological-insulator class with a single Dirac cone on the surface. *Nat. Phys.* **2009**, *5*, 398−402.

(5) Liu, Z. K.; et al. A stable three-dimensional topological Dirac semimetal Cd_3As_2. *Nat. Mater.* **2014**, *13*, 677−681.

(6) Xu, S.-Y.; et al. Observation of Fermi arc surface states in a topological metal. *Science* **2015**, *347*, 294−298.

(7) Xu, S.-Y.; et al. Discovery of a Weyl fermion semimetal and topological Fermi arcs. *Science* **2015**, *349*, 613−617.

(8) Lv, B.; Qian, T.; Ding, H. Angle-resolved photoemission spectroscopy and its application to topological materials. *Nat. Rev. Phys.* **2019**, *1*, 609−626.

(9) Krieger, J. A.; et al. Weyl spin-momentum locking in a chiral topological semimetal. *Nat. Commun.* **2024**, *15*, 3720.

(10) Boschini, F.; Zonno, M.; Damascelli, A. Time-resolved ARPES studies of quantum materials. *Rev. Mod. Phys.* **2024**, *96*, 015003.

(11) Dai, Y. M.; Bowlan, J.; Li, H.; Miao, H.; Wu, S. F.; Kong, W. D.; Richard, P.; Shi, Y. G.; Trugman, S. A.; Zhu, J.-X.; Ding, H.; Taylor, A. J.; Yarotski, D. A.; Prasankumar, R. P. Ultrafast carrier dynamics in the large-magnetoresistance material WTe_2. *Phys. Rev. B* **2015**, *92*, 161104.

(12) Crepaldi, A.; et al. Enhanced ultrafast relaxation rate in the Weyl semimetal phase of $MoTe_2$ measured by time- and angle-resolved photoelectron spectroscopy. *Phys. Rev. B* **2017**, *96*, 241408.

(13) Hein, P.; Jauernik, S.; Erk, H.; Yang, L.; Qi, Y.; Sun, Y.; Felser, C.; Bauer, M. Mode-resolved reciprocal space mapping of electron-phonon interaction in the Weyl semimetal candidate Td-WTe2. *Nat. Commun.* **2020**, *11*, 2613.

(14) Beaulieu, S.; Dong, S.; Tancogne-Dejean, N.; Dendzik, M.; Pincelli, T.; Maklar, J.; Xian, R. P.; Sentef, M. A.; Wolf, M.; Rubio, A.; Rettig, L.; Ernstorfer, R. Ultrafast dynamical Lifshitz transition. *Sci. Adv.* **2021**, *7*, No. eabd9275.

(15) Sobota, J. A.; Yang, S.; Analytis, J. G.; Chen, Y. L.; Fisher, I. R.; Kirchmann, P. S.; Shen, Z.-X. Ultrafast Optical Excitation of a Persistent Surface-State Population in the Topological Insulator Bi_2Se_3. *Phys. Rev. Lett.* **2012**, *108*, 117403.

(16) Wang, X.-P.; Richard, P.; Huang, Y.-B.; Miao, H.; Cevey, L.; Xu, N.; Sun, Y.-J.; Qian, T.; Xu, Y.-M.; Shi, M.; Hu, J.-P.; Dai, X.; Ding, H. Orbital characters determined from Fermi surface intensity patterns using angle-resolved photoemission spectroscopy. *Phys. Rev. B* **2012**, *85*, 214518.

(17) Reimann, J.; Güdde, J.; Kuroda, K.; Chulkov, E. V.; Höfer, U. Spectroscopy and dynamics of unoccupied electronic states of the topological insulators Sb_2Te_3 and Sb_2Te_2S. *Phys. Rev. B* **2014**, *90*, 081106.

(18) Zhu, S.; Ishida, Y.; Kuroda, K.; Sumida, K.; Ye, M.; Wang, J.; Pan, H.; Taniguchi, M.; Qiao, S.; Shin, S.; Kimura, A. Ultrafast electron dynamics at the Dirac node of the topological insulator Sb_2Te_3. *Sci. Rep.* **2015**, *5*, 13213.

(19) Herb, M.; Weigl, L.; Hofman, N.; Gradl, J.; Khoury, J. F.; Schoop, L.; Gierz, I. Direct evidence for efficient carrier multiplication

in the topological insulator Bi_2Se_3. *arXiv (cond-mat.mtrl-sci)*, Submission Date: 2024−05−02, DOI: 10.48550/arXiv.2405.01323 (accessed 2024−07−10).
(20) Gierz, I.; Petersen, J. C.; Mitrano, M.; Cacho, C.; Turcu, I. C. E.; Springate, E.; Stöhr, A.; Köhler, A.; Starke, U.; Cavalleri, A. Snapshots of non-equilibrium Dirac carrier distributions in graphene. *Nat. Mater.* **2013**, *12*, 1119−1124.
(21) Gierz, I.; Mitrano, M.; Bromberger, H.; Cacho, C.; Chapman, R.; Springate, E.; Link, S.; Starke, U.; Sachs, B.; Eckstein, M.; Wehling, T. O.; Katsnelson, M. I.; Lichtenstein, A.; Cavalleri, A. Phonon-Pump Extreme-Ultraviolet-Photoemission Probe in Graphene: Anomalous Heating of Dirac Carriers by Lattice Deformation. *Phys. Rev. Lett.* **2015**, *114*, 125503.
(22) Choi, D.; Mogi, M.; De Giovannini, U.; Azoury, D.; Lv, B.; Su, Y.; Hübener, H.; Rubio, A.; Gedik, N. Direct observation of Floquet-Bloch states in monolayer graphene. *arXiv (cond-mat.mes-hall)*, Submission Date: 2024−04−22, DOI: 10.48550/arXiv.2404.14392 (accessed 2024−07−10).
(23) Merboldt, M.; Schüler, M.; Schmitt, D.; Bange, J. P.; Bennecke, W.; Gadge, K.; Pierz, K.; Schumacher, H. W.; Momeni, D.; Steil, D.; Manmana, S. R.; Sentef, M.; Reutzel, M.; Mathias, S. Observation of Floquet states in graphene. *arXiv (cond-mat.mes-hall)*, Submission Date: 2024−04−19, DOI: 10.48550/arXiv.2404.12791 (accessed 2024−07−10).
(24) Bao, C.; Li, Q.; Xu, S.; Zhou, S.; Zeng, X.-Y.; Zhong, H.; Gao, Q.; Luo, L.; Sun, D.; Xia, T.-L.; Zhou, S. Population inversion and Dirac fermion cooling in 3D Dirac semimetal Cd_3As_2. *Nano Lett.* **2022**, *22*, 1138−1144.
(25) Lin, T.; Ju, Y.; Zhong, H.; Zeng, X.; Dong, X.; Bao, C.; Zhang, H.; Xia, T.-L.; Tang, P.; Zhou, S. Ultrafast carrier relaxation dynamics in a nodal-line semimetal $PtSn_4$. *Nano Lett.* **2024**, *24*, 6278−6285.
(26) Fragkos, S.; Tsipas, P.; Xenogiannopoulou, E.; Panayiotatos, Y.; Dimoulas, A. Type-III Dirac fermions in $Hf_xZr_{1x}Te_2$ topological semimetal candidate. *J. Appl. Phys.* **2021**, *129*, 075104.
(27) Tsipas, P.; Tsoutsou, D.; Fragkos, S.; Sant, R.; Alvarez, C.; Okuno, H.; Renaud, G.; Alcotte, R.; Baron, T.; Dimoulas, A. Massless Dirac fermions in $ZrTe_2$ semimetal grown on InAs(111) by van der Waals epitaxy. *ACS Nano* **2018**, *12*, 1696−1703.
(28) Kar, I.; Chatterjee, J.; Harnagea, L.; Kushnirenko, Y.; Fedorov, A. V.; Shrivastava, D.; Büchner, B.; Mahadevan, P.; Thirupathaiah, S. Metal-chalcogen bond-length induced electronic phase transition from semiconductor to topological semimetal in ZrX_2 (X = Se and Te). *Phys. Rev. B* **2020**, *101*, DOI: 10.1103/PhysRevB.101.165122
(29) Nguyen, T.; Aryal, N.; Pokharel, B. K.; Harnagea, L.; Mierstchin, D.; Popović, D.; Graf, D. E.; Shrestha, K. Fermiology of the Dirac type-II semimetal candidates $(Ni,Zr)Te_2$ using de Haas−van Alphen oscillations. *Phys. Rev. B* **2022**, *106*, 075154.
(30) Zhang, B.; Muhammad, Z.; Wang, P.; Cui, S.; Li, Y.; Wang, S.; Wu, Y.; Liu, Z.; Zhu, H.; Liu, Y.; Zhang, G.; Liu, D.; Song, L.; Sun, Z. Electronic structures of Cr-intercalated $ZrTe_2$ revealed by angle-resolved photoemission spectroscopy. *J. Phys. Chem. C Nanomater. Interfaces* **2020**, *124*, 16561−16567.
(31) Ng, S. M.; Wang, H.; Liu, Y.; Wong, H. F.; Yau, H. M.; Suen, C. H.; Wu, Z. H.; Leung, C. W.; Dai, J.-Y. High-temperature anomalous Hall effect in a transition metal dichalcogenide ferromagnetic insulator heterostructure. *ACS Nano* **2020**, *14*, 7077−7084.
(32) Wang, H.; Chan, C. H.; Suen, C. H.; Lau, S. P.; Dai, J.-Y. Magnetotransport properties of layered topological material $ZrTe_2$ thin film. *ACS Nano* **2019**, *13*, 6008−6016.
(33) Ou, Y.; Yanez, W.; Xiao, R.; Stanley, M.; Ghosh, S.; Zheng, B.; Jiang, W.; Huang, Y.-S.; Pillsbury, T.; Richardella, A.; Liu, C.; Low, T.; Crespi, V. H.; Mkhoyan, K. A.; Samarth, N. $ZrTe_2/CrTe_2$: an epitaxial van der Waals platform for spintronics. *Nat. Commun.* **2022**, *13*, 2972.
(34) Bradlyn, B.; Elcoro, L.; Cano, J.; Vergniory, M. G.; Wang, Z.; Felser, C.; Aroyo, M. I.; Bernevig, B. A. Topological quantum chemistry. *Nature* **2017**, *547*, 298−305.
(35) Comby, A.; Rajak, D.; Descamps, D.; Petit, S.; Blanchet, V.; Mairesse, Y.; Gaudin, J.; Beaulieu, S. Ultrafast polarization-tunable monochromatic extreme ultraviolet source at high-repetition-rate. *Journal of Optics* **2022**, *24*, 084003.
(36) Tkach, O. et al. Multi-Mode Front Lens for Momentum Microscopy: Part II Experiments. *arXiv (cond-mat.mtrl-sci)*, Submission Date:2024−01−19, DOI: 10.48550/arXiv.2401.10084 (accessed 2024−07−10).
(37) Sterzi, A.; Manzoni, G.; Crepaldi, A.; Cilento, F.; Zacchigna, M.; Leclerc, M.; Bugnon, P.; Magrez, A.; Berger, H.; Petaccia, L.; Parmigiani, F. Probing band parity inversion in the topological insulator $GeBi_2Te_4$ by linear dichroism in ARPES. *J. Electron Spectrosc. Relat. Phenom.* **2018**, *225*, 23−27.
(38) Bentmann, H.; et al. Profiling spin and orbital texture of a topological insulator in full momentum space. *Phys. Rev. B* **2021**, *103*, L161107.
(39) Beaulieu, S.; Schusser, J.; Dong, S.; Schüler, M.; Pincelli, T.; Dendzik, M.; Maklar, J.; Neef, A.; Ebert, H.; Hricovini, K.; Wolf, M.; Braun, J.; Rettig, L.; Minár, J.; Ernstorfer, R. Revealing Hidden Orbital Pseudospin Texture with Time-Reversal Dichroism in Photoelectron Angular Distributions. *Phys. Rev. Lett.* **2020**, *125*, 216404.
(40) Beaulieu, S.; Schüler, M.; Schusser, J.; Dong, S.; Pincelli, T.; Maklar, J.; Neef, A.; Reinert, F.; Wolf, M.; Rettig, L.; Minár, J.; Ernstorfer, R. Unveiling the orbital texture of 1T-$TiTe_2$ using intrinsic linear dichroism in multidimensional photoemission spectroscopy. *Npj Quantum Mater.* **2021**, *6*, 93.
(41) Cho, S.; Park, J.-H.; Hong, J.; Jung, J.; Kim, B. S.; Han, G.; Kyung, W.; Kim, Y.; Mo, S.-K.; Denlinger, J. D.; Shim, J. H.; Han, J. H.; Kim, C.; Park, S. R. Experimental Observation of Hidden Berry Curvature in Inversion-Symmetric Bulk 2*H*-WSe_2. *Phys. Rev. Lett.* **2018**, *121*, 186401.
(42) Schüler, M.; De Giovannini, U.; Hübener, H.; Rubio, A.; Sentef, M. A.; Werner, P. Local Berry curvature signatures in dichroic angle-resolved photoelectron spectroscopy from two-dimensional materials. *Sci. Adv.* **2020**, *6*, No. eaay2730.
(43) Cho, S.; Park, J.-H.; Huh, S.; Hong, J.; Kyung, W.; Park, B.-G.; Denlinger, J. D.; Shim, J. H.; Kim, C.; Park, S. R. Studying local Berry curvature in 2H-WSe2 by circular dichroism photoemission utilizing crystal mirror plane. *Sci. Rep.* **2021**, *11*, 1684.
(44) Schüler, M.; Pincelli, T.; Dong, S.; Devereaux, T. P.; Wolf, M.; Rettig, L.; Ernstorfer, R.; Beaulieu, S. Polarization-modulated angle-resolved photoemission spectroscopy: Toward circular dichroism without circular photons and Bloch wave-function reconstruction. *Phys. Rev. X* **2022**, *12*, 011019.
(45) Yan, M.; et al. Lorentz-violating type-II Dirac fermions in transition metal dichalcogenide $PtTe_2$. *Nat. Commun.* **2017**, *8*, 257.
(46) Sie, E. J.; Rohwer, T.; Lee, C.; Gedik, N. Time-resolved XUV ARPES with tunable 24−33 eV laser pulses at 30 meV resolution. *Nat. Commun.* **2019**, *10*, 3535.
(47) Guo, Q.; Dendzik, M.; Grubišić-Čabo, A.; Berntsen, M. H.; Li, C.; Chen, W.; Matta, B.; Starke, U.; Hessmo, B.; Weissenrieder, J.; Tjernberg, O. A narrow bandwidth extreme ultra-violet light source for time- and angle-resolved photoemission spectroscopy. *Structural Dynamics* **2022**, *9*, 024304.
(48) Heber, M.; Wind, N.; Kutnyakhov, D.; Pressacco, F.; Arion, T.; Roth, F.; Eberhardt, W.; Rossnagel, K. Multispectral time-resolved energy−momentum microscopy using high-harmonic extreme ultraviolet radiation. *Rev. Sci. Instrum.* **2022**, *93*, 083905.
(49) Chen, F.; Wang, J.; Pan, M.; Liu, J.; Huang, J.; Zhao, K.; Yun, C.; Qian, T.; Wei, Z.; Ding, H. Time-resolved ARPES with tunable 12−21.6 eV XUV at 400 kHz repetition rate. *Rev. Sci. Instrum.* **2023**, *94*, 043905.
(50) Majchrzak, P.; Zhang, Y.; Kuibarov, A.; Chapman, R.; Wyatt, A.; Springate, E.; Borisenko, S.; Büchner, B.; Hofmann, P.; Sanders, C. E. Access to the full three-dimensional Brillouin zone with time resolution, using a new tool for pump−probe angle-resolved photoemission spectroscopy. *Rev. Sci. Instrum.* **2024**, *95*, 063001.
(51) Majchrzak, P.; Sanders, C.; Zhang, Y.; Kuibarov, A.; Suvorov, O.; Springate, E.; Kovalchuk, I.; Aswartham, S.; Shipunov, G.; Büchner, B.; Yaresko, A.; Borisenko, S.; Hofmann, P. Ultrafast carrier dynamics throughout the three-dimensional Brillouin zone of the

Weyl semimetal $PtBi_2$. *arXiv (cond-mat.str-el)*, 2024 DOI: 10.48550/arXiv.2406.10550.
(52) Caputo, M.; Khalil, L.; Papalazarou, E.; Nilforoushan, N.; Perfetti, L.; Taleb-Ibrahimi, A.; Gibson, Q. D.; Cava, R. J.; Marsi, M. Dynamics of out-of-equilibrium electron and hole pockets in the type-II Weyl semimetal candidate WTe_2. *Phys. Rev. B* **2018**, *97*, 115115.
(53) González, J.; Guinea, F.; Vozmediano, M. A. H. Unconventional Quasiparticle Lifetime in Graphite. *Phys. Rev. Lett.* **1996**, *77*, 3589−3592.
(54) Mor, S.; Herzog, M.; Monney, C.; Stähler, J. Ultrafast charge carrier and exciton dynamics in an excitonic insulator probed by time-resolved photoemission spectroscopy. *Prog. Surf. Sci.* **2022**, *97*, 100679.

NOTE ADDED AFTER ISSUE PUBLICATION

This paper was originally published ASAP on October 10, 2024, and included in volume 24, issue 42. The Acknowledgments were updated to include funding from LASERLAB-EUROPE, and the paper was reposted on November 25, 2024.

https://doi.org/10.1021/acs.nanolett.4c04019
Nano Lett. 2024, 24, 13397−13404